ADVANCED FUNCTIONAL MATERIALS
www.afm-journal.de

Nanocasting of Mesoporous In-TM (TM = Co, Fe, Mn) Oxides: Towards 3D Diluted-Oxide Magnetic Semiconductor Architectures

Eva Pellicer, Moisés Cabo, Emma Rossinyol, Pau Solsona, Santiago Suriñach, Maria Dolors Baró, and Jordi Sort**

Transition metal (Co, Fe, Mn)-doped In_2O_{3-y} mesoporous oxides are synthesized by nanocasting using mesoporous silica as hard templates. 3D ordered mesoporous replicas are obtained after silica removal in the case of the In-Co and In-Fe oxide powders. During the conversion of metal nitrates into the target mixed oxides, Co, Fe, and Mn ions enter the lattice of the In_2O_3 bixbyite phase via isovalent or heterovalent cation substitution, leading to a reduction in the cell parameter. In turn, non-negligible amounts of oxygen vacancies are also present, as evidenced from Rietveld refinements of the X-ray diffraction patterns. In addition to $(In_{1-x}TM_x)_2O_{3-y}$, minor amounts of Co_3O_4, α-Fe_2O_3, and Mn_xO_y phases are also detected, which originate from the remaining TM cations not forming part of the bixbyite lattice. The resulting TM-doped In_2O_{3-y} mesoporous materials show a ferromagnetic response at room temperature, superimposed on a paramagnetic background. Conversely, undoped In_2O_{3-y} exhibits a mixed diamagnetic-ferromagnetic behavior with much smaller magnetization. The influence of the oxygen vacancies and the doping elements on the magnetic properties of these materials is discussed. Due to their 3D mesostructural geometrical arrangement and their room-temperature ferromagnetic behavior, mesoporous oxide-diluted magnetic semiconductors may become smart materials for the implementation of advanced components in spintronic nanodevices.

1. Introduction

With the advent of nanotechnology, the search for advanced methods for the processing of complex metal oxides and double oxides with precise control at the nanoscale has elicited enormous interest. Several synthetic routes have been put forward to produce nanoparticles, nanorods, and nanowires of these materials, aimed at exploiting the unique properties derived from their small size.[1,2] Among the synthesis pathways leading to nanostructured oxide-based materials, the nanocasting route constitutes a versatile technique to obtain many simple transition metal (TM) mesoporous oxides as negative replicas of mesoporous silica or carbon hard templates. The successful synthesis of nanocrystalline Co_3O_4, CeO_2, WO_3, In_2O_3, NiO, Fe_2O_3, among others, with different pore network topologies (SBA-15, KIT-6, FDU-1, MCM-41, etc.) has been demonstrated in recent years.[3] Metal oxides obtained in this way benefit from large surface-to-volume ratios provided by an ordered arrangement of mesopores. Recently, the nanocasting pathway has been extended to prepare oxides containing two different metal (M, M′) cations, such as spinel-type $MM_2'O_4$, and double oxides. With this aim, the hard template is filled with a mixture of precursors in the appropriate ratio. Upon calcining, the precursors are converted to the target materials, which are finally released by selective etching of the silica host with either NaOH or HF solutions. Following this approach, several spinels ($NiCo_2O_4$, $MnCo_2O_4$, $NiFe_2O_4$, $CoFe_2O_4$, $CuAl_2O_4$) have been obtained,[4–8] as well as double oxides (Al-Ti oxides[9] or Cu-Ce oxides),[10] or even more complex systems like NiO-Co_3O_4-$NiCo_2O_4$ mesoporous nanocomposites.[11]

The interest in mesoporous oxide materials is fostered by their widespread technological applications in diverse areas such as heterogeneous catalysis,[12] gas sensors,[13] solid electrolytes for rechargeable batteries,[14,15] supercapacitors[16] or optoelectronic devices,[17] amongst others. Some of these mesoporous oxides (e.g., TM-oxides) also show ferromagnetic or ferrimagnetic behavior at room temperature.[11]

Dr. E. Pellicer, M. Cabo, Dr. P. Solsona, Prof. S. Suriñach, Prof. M. D. Baró
Departament de Física
Facultat de Ciències
Universitat Autònoma de Barcelona
E-08193 Bellaterra, Spain
E-mail: Eva.Pellicer.icn@uab.cat
Dr. E. Rossinyol
Servei de Microscòpia
Facultat de Ciències
Universitat Autònoma de Barcelona
E-08193 Bellaterra, Spain
Prof. J. Sort
Institució Catalana de Recerca i Estudis Avançats (ICREA)
and Departament de Física
Facultat de Ciències
Universitat Autònoma de Barcelona
E-08193 Bellaterra, Spain
E-mail: Jordi.Sort@uab.cat

DOI: 10.1002/adfm.201201486

© 2013 WILEY-VCH Verlag GmbH & Co. KGaA, Weinheim

Compared with other metal oxides, In_2O_3 is particularly easy to replicate.[3] SBA-15- and KIT-6-templated In_2O_3 materials displaying long-range order and relatively large surface-to-volume ratios can be obtained by using indium nitrate salt as a precursor.[18] By varying the precursor/template molar ratio it is possible to obtain either nanoparticles, nanorods, or perfectly arranged nanowires.[19,20] The multifunctional applications of mesoporous In_2O_3 have been demonstrated in several pieces of work. For example, as a gas sensor, this material allows efficient detection of small concentrations of CO_2, CH_4, HCHO, or H_2O.[21–24] Moreover, photoluminescence phenomena different from that encountered in In_2O_3 films and powders have been reported in In_2O_3 nanoparticles homogeneously dispersed within the pores of mesoporous silica.[25] Furthermore, In_2O_3-Co_3O_4 and In_2O_3-Fe_2O_3 nonporous composite powders show enhanced sensing performance towards various gases, as compared with pure In_2O_3.[26,27]

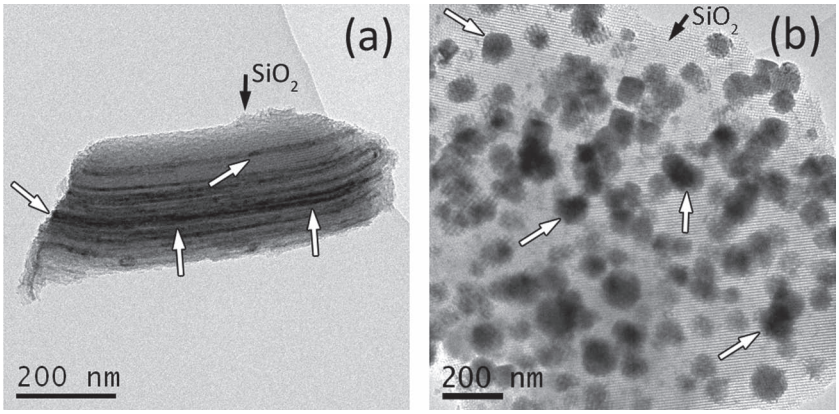

Figure 1. a,b) TEM images of SBA-15 (a) and KIT-6 (b) silica filled with Co-doped In_2O_3 oxides. The target products embedded inside the SiO_2 mesoporous matrices are indicated by the white arrows.

Remarkably, semiconductor films composed of In_2O_3 doped with a TM (Co, Fe, Mn or Cr) belong to the so-called oxide-diluted magnetic semiconductors (ODMSs), which combine the interesting electronic properties of semiconductors with room-temperature ferromagnetism.[28–38] Other examples are TM-doped ZnO, SnO_2, or TiO_2. These materials are appealing for spintronic applications, where both the spin and the charge of electrons are intended to be used for the storage and processing of information. Furthermore, In_2O_3 is a transparent semiconductor with potential applications in the field of magneto-optics (i.e., the Faraday effect). Doping In_2O_3 with a suitable TM has been proposed as an appealing method of manufacturing ferromagnetic transparent conducting oxide structures with a high Curie temperature.[37,38]

Most ODMSs reported so far have been prepared as continuous thin films, bulk materials or coarse polycrystalline powders. Although there are a few studies on the growth of ODMS nanoparticles[39] and nanowires,[40] the synthesis of 3D mesoporous ODMS structures by hard-templating has not been reported so far. Engineering 3D magnetic semiconductor architectures with ordered arrangements would be highly desirable, not only to obtain novel magnetic and optical properties but also to develop key components in spintronic nanodevices. Indeed, the control of the size, shape, and orientation of semiconductor nanocrystallites allows the precise tuning of their physicochemical properties.[41] Porous ODMS frameworks would exhibit a combination of unique properties including coupled electronic/magnetic/photocatalytic properties, quantum-confinement effects, a high internal surface area for absorption purposes, or the possibility of filling the internal pores with secondary phases (oxides or metals) to yield hybrid nanocomposites with synergic functionalities. The ability to precisely align and orient these materials to form large, ordered 3D arrays with controlled geometries would therefore represent a significant breakthrough in spintronic storage technologies.

The origin of room-temperature ferromagnetism in ODMSs remains to some extent still controversial, although it has been claimed to arise both from the dilution of 3d elements in the crystallographic structure and from the presence of structural defects (e.g., oxygen vacancies).[28–35,42–44] In some cases, oxide semiconductors can be ferromagnetic even in the undoped states.[45] Conversely, in other studies, only paramagnetic behavior has been reported in ODMSs, regardless of the dilution state.[46] Hence, conclusive studies on the detailed correlation between the dilution level, the amount and type of defects, and the generated ferromagnetic response are still lacking.

In this work, we explore the synthesis of Co-, Fe-, and Mn-doped In_2O_3 mesoporous oxides by nanocasting using SBA-15 and KIT-6 silica as hard templates. The obtained mesoporous materials are compared in terms of their morphology, surface area, crystallographic structure of the constituent phases, and magnetic properties. It is shown that both the TM species and the type of mesoporous structure have a key influence on the obtained ferromagnetic/paramagnetic properties, which are controlled by both the doping state and the amount of oxygen vacancies.

2. Results and Discussion

2.1. Morphological Characterization

Representative transmission electron microscopy (TEM) images of the SBA-15 and KIT-6 silica templates filled with Co-In oxide, acquired after precursor impregnation and calcination and prior to the template removal step, are shown in **Figure 1**. The darker regions correspond to the In-Co oxide target products (indicated by the white arrows) confined within the silica channels, which look brighter when empty. The morphology of the replicas obtained after selective etching of the silica hosts is shown in **Figure 2**. Remarkably, no non-mesoporous (i.e., bulk) particles were observed, either before or after silica removal, suggesting a good impregnation of the silica templates. The size of the metal oxide replica particles (e.g., between 100 and 200 nm in the KIT-6 replicas, see Figure 1b) was typically smaller than the size of the parent silica particles, which reached values in excess of 0.5 μm (see Supporting Information, Figure S1). Such a difference is ascribed to the volume change occurring during

© 2013 WILEY-VCH Verlag GmbH & Co. KGaA, Weinheim

conversion of precursors into the target oxide products. Namely, a reduction in the fraction of occupied silica voids takes place on calcining, an effect which can be defined according to the volume contraction ratio:[3]

$$\text{Volume contraction ratio} = \frac{\text{Volume of the target product}}{\text{Volume of precursor}} \quad (1)$$

where:

$$\text{Volume of the target product} = \frac{\text{Molecular weight of the target product}}{\text{Density of the target product}} \quad (2)$$

$$\text{Volume of precursor} = \frac{n \times \text{Molecular weight of precursor}}{\text{Density of precursor}} \quad (3)$$

Here, n represents the number of precursor molecules that transform into one target product molecule.

The volume contraction ratio for TM nitrate salts into the corresponding target oxides is typically between 6% and 11%.[3] Hence, assuming that 100% of mesopores are fully filled with the precursors after the impregnation step, only around 6–11% of voids remain filled after their chemical conversion into the target oxides. The released SBA-15 templated In-Co and In-Fe oxides were composed of ordered nanowire arrays (see Figure 2a and 2c). The diameter of the nanowires, as estimated from high-resolution TEM images, was around 7–8 nm, in agreement with the pore size of the parent template (see Figure 2e and inset in Supporting Information, Figure S1a). Their length varied significantly as a function of the precursor used. Longer nanowires were observed in the In-Co and In-Fe samples, whereas shorter ones were formed in the In-Mn mixed oxide. To be precise, the In-Mn oxide replica was actually constructed from randomly oriented nanorods, thus lacking long-range order (see Supporting Information, Figure S2). This phenomenon can be ascribed, at least in part, to the low diffusion coefficient of Mn^{2+} onto silica surfaces, which precludes a good replication of the pore network, ultimately leading to disordered pore walls. It has been proposed that the diffusion kinetics of metal cations onto the silica pores determines the success in the replication to some extent; so that the higher the diffusion coefficient of the cation, the better is the replication of the mesostructural features of the silica host.[3]

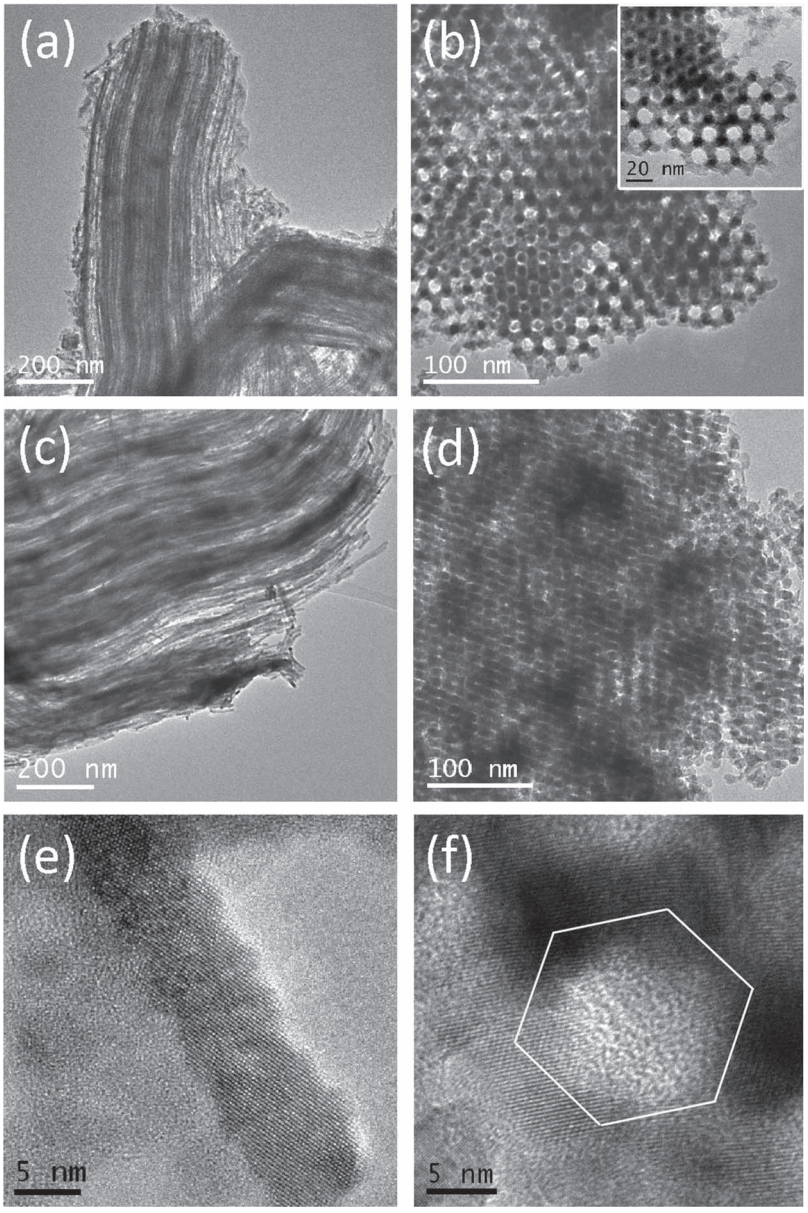

Figure 2. a–d) TEM images of the TM-doped In_2O_3 oxides obtained after SBA-15 silica removal for TM = Co (a) and TM = Fe (c), and after KIT-6 silica removal for TM = Co (b) and TM = Fe (d). e,f) High-resolution TEM images of Co-doped In_2O_3 in the SBA-15 mesostructure (e), showing the detail of a single nanowire, and KIT-6 mesostructure (f), featuring the hexagonal ring typical of this bicontinuous gyroid structure.

Concerning the KIT-6 replicas, similar trends as for the SBA-15 templating process were observed. The particles exhibited, however, a roughly spherical morphology (see Figure 2b,d). Such a spherical shape was already evident in the filled KIT-6 silicas (Figure 1b). Both In-Co and In-Fe replicas featured a bicontinuous cubic mesostructure (*Ia3d* symmetry), with two sets of nanowires helically twisted with respect to each other in a periodical manner. A magnified image displaying the characteristic hexagonal pore structure is shown in the inset of Figure 2b, while a corresponding high-resolution TEM image is presented in Figure 2f. Field-emission scanning electron microscopy (FE-SEM) images of the KIT-6 templated In-Co oxide powders are shown in **Figure 3**, where the rather spherical shape of the particles is again evidenced. Similar to the SBA-15 case, the mesoporous structure is less evident in the In-Mn oxide replica (see Supporting Information, Figure S2). This indicates that the templating process using the manganese nitrate precursor involves some difficulties, which makes the nanocasting synthesis for this particular case less successful.

© 2013 WILEY-VCH Verlag GmbH & Co. KGaA, Weinheim

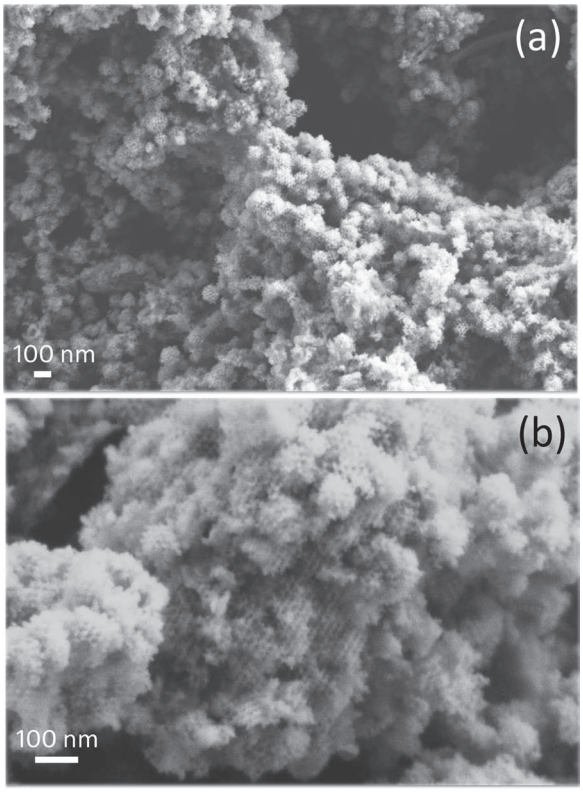

Figure 3. a,b) Low-magnification (a) and high-magnification (b) FE-SEM images of KIT-6 templated Co-doped In_2O_3 oxide replica.

It is worth mentioning that while In_2O_3 and Co_3O_4 are easy to replicate, the nanocasting synthesis of α-Fe_2O_3 and Mn_xO_y has proven to be generally more challenging.[47,48] Indeed, it is known that the formation of mesoporous metal oxides with noncubic crystallographic structures, such as rhombic α-Fe_2O_3 or tetragonal MnO_2, involves difficulties in terms of replication of the 3D mesopore geometry.[3] Therefore, the presence of indium nitrate precursor, combined with iron nitrate, probably favors the formation of the ordered In-Fe oxide mesophases by increasing the mesoscopic regularity.

Figure 4 shows the adsorption-desorption N_2 curves for In-Co, In-Fe, and In-Mn oxide powders after silica removal. It can be seen that the profile curves are different, depending on both the doping TM element and the parent silica host. The corresponding Barrett–Joyner–Hallenda (BJH) pore-size distributions in the mesopore domain (up to 50 nm) are plotted in the Supporting Information, Figure S3. For the Co-In samples, step adsorption and H1-type hysteresis at P/P_0 in the range of 0.4–0.8 can be observed. This has been associated with the filling and emptying of mesopores by capillary condensation.[5] At P/P_0 values close to 1, the amount of N_2 rapidly increases, indicating the presence of large interparticle voids (i.e., textural porosity).[22] Hence, the obtained materials consist of not only arranged mesopores (inner porosity), but also disordered interparticle voids as a result of partial structural collapse probably occurring during the annealing process. Unlike the In-Co powders, the In-Fe samples show a pronounced uptake at 0.8–0.9 P/P_0. The corresponding BJH distribution gives a maximum in the pore-size distribution centered at 15 nm, which is larger than for the In-Co systems (see Supporting Information, Figure S3). Finally, the In-Mn powders show a type-I isotherm with an H4 hysteresis loop, which indicates the presence of large mesopores, as well as a large fraction of interparticle voids. The corresponding pore-size distributions are indeed shifted towards higher values compared with those for In-Co and In-Fe. The Brunauer–Emmet–Teller (BET) surface areas are in the range of 50–100 $m^2\ g^{-1}$ (see **Table 1**). The negative slope at intermediate values of P/P_0 in Figure 4e might be due to slight under-pressurization within this range.

The low-angle X-ray diffraction (XRD) patterns of the nanocast oxides synthesized using the SBA-15 and KIT-6 silica mesostructures as hard templates are shown in **Figure 5**. The (100) peak from the *p6mm* hexagonal symmetry of the SBA-15 structure is visible, particularly for the undoped In_2O_3 and the In-Co and In-Fe oxides, while a shoulder corresponding to the (110) reflection is also seen for Mn-doped In_2O_3 (see Figure 5a). Similarly, the (211) peak of the *Ia-3d* KIT-6 cubic symmetry can be clearly identified for the undoped In_2O_3 and the In-Co and In-Fe oxides. Conversely, no clear peaks can be seen in the small-angle XRD patterns of the Mn-In oxides. These results indicate that the long-range order is preserved to some extent in undoped In_2O_3 and in In-Co and In-Fe oxides. In fact, their low-angle signatures are very similar to those reported for TM oxides synthesized by hard templating through a single impregnation step.[5,11,49] On the contrary, the mesoporous order is essentially lost during replication of the In-Mn oxides, in agreement with the TEM observations.

2.2. Structural (Crystallographic) Characterization

In order to determine the influence of the TM doping elements on the crystallographic structure of the In_2O_3 phase, as well as to seek additional phases eventually formed in the mesoporous oxides, a detailed wide-angle XRD investigation, including full-pattern Rietveld refinements of the XRD patterns, was performed. The wide-angle XRD patterns of KIT-6 templated In-TM oxides are shown in **Figure 6**b–d. For comparison, the diffractogram corresponding to pure In_2O_3 KIT-6 replica is also displayed (Figure 6a). Similar profiles were observed for the SBA-15 templated replicas (Supporting Information, Figure S4). The detail of the XRD patterns of SBA-15 In-TM oxides in the angular range from $2\theta = 47.5°$ to 65° is shown in **Figure 7**a.

Several observations can be qualitatively made from the shape of the XRD patterns. First, no hump was present at $2\theta \approx 20°$, confirming the successful elimination of the SiO_2 template. Actually, the silicon content was below 1 wt%, as determined from energy dispersive X-ray (EDX) compositional analyses. The pattern of pure In_2O_3 shows the characteristic peaks of cubic bixbyite (*Ia3* space group, JCPDF No. 71–2194), which contains two crystallographically unique cation sites, 24*d* (In2) and 8*b* (In1), according to Wyckoff's notation. In addition to the bixbyite-type phase, secondary phases were also detected in minor amounts, particularly in the KIT-6 mesoporous structures (see Figure 6 and Figure 7b). These secondary phases were: cubic Co_3O_4 spinel (JCPDF No. 71–0816) for the

© 2013 WILEY-VCH Verlag GmbH & Co. KGaA, Weinheim

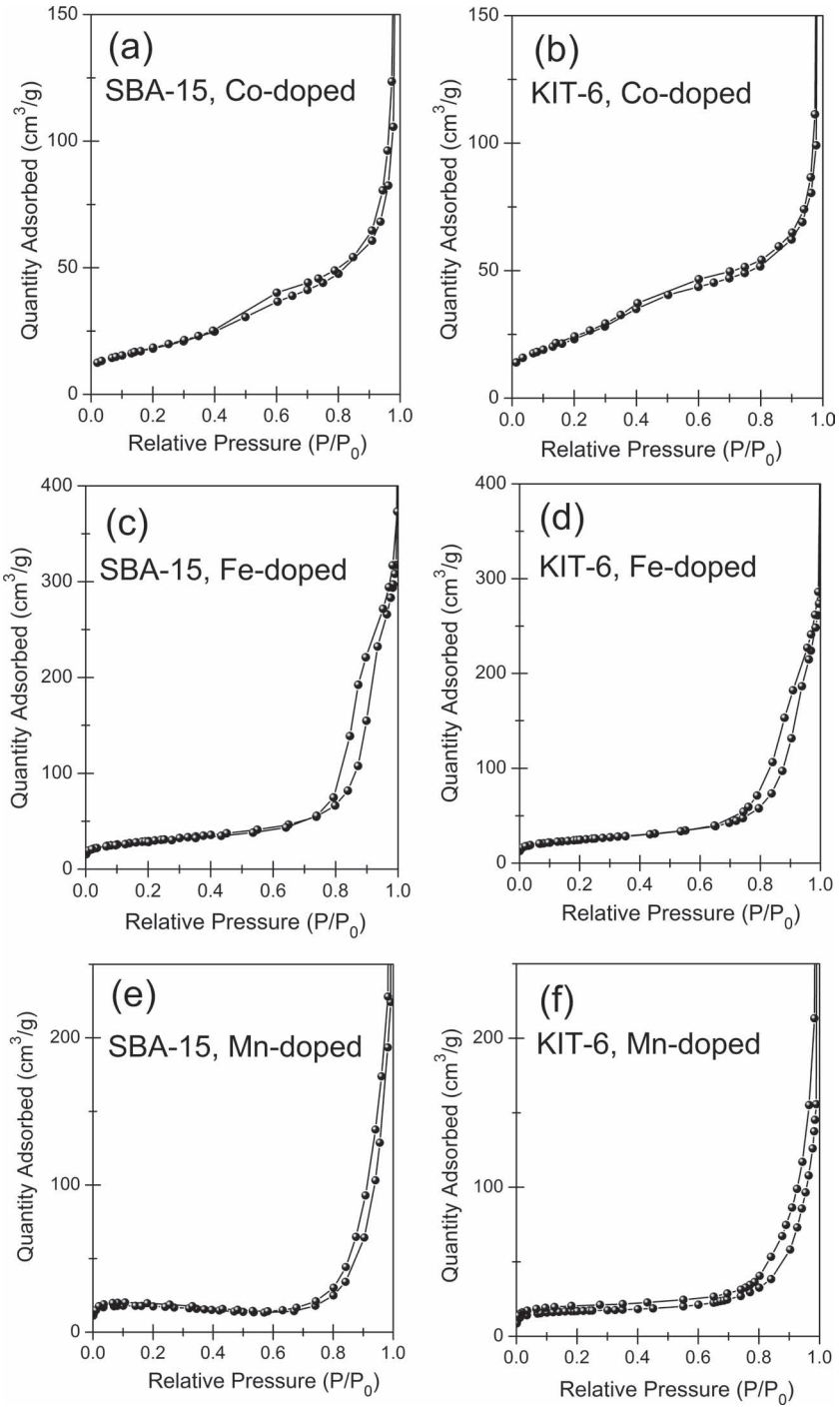

Figure 4. a–f) N_2 adsorption-desorption isotherms for TM-doped In_2O_3 oxides obtained after SBA-15 silica removal for TM = Co (a), TM = Fe (c), and TM = Mn (e); and after KIT-6 silica removal for TM = Co (b), TM = Fe (d), and TM = Mn (f).

In-Co oxides, α-Fe_2O_3 phase (JCPDF No. 33–0663) for the In-Fe oxides, and a mixture of Mn_xO_y phases for the In-Mn oxides. It should be noted that the formation of a single Co_3O_4 phase during nanocasting from a cobalt nitrate precursor is well established.[50] In turn, the synthesis of an α-Fe_2O_3 single phase by hard templating using iron nitrate has been also reported previously.[47] Conversely, mixtures of MnO_2, Mn_2O_3, and Mn_3O_4 oxides have been detected in the hard-templating synthesis using manganese nitrate as precursor.[51] It is worth mentioning that the stoichiometric $CoIn_2O_4$ spinel structure was not formed under our experimental conditions, in spite of using a 2:1 In(III):Co(II) molar ratio in the impregnation step. The existence of unconventional ternary cobalt spinels oxides, CoX_2O_4 (X = Al, Ga, In), has been recently theoretically predicted by thermodynamic considerations and experimental work trying to produce these phases in thin-film form has been performed by radio-frequency (RF) magnetron sputtering.[52] However, while the successful synthesis of pure $CoGa_2O_4$ and $CoAl_2O_4$ films was demonstrated, attempts to produce $InCo_2O_4$ failed. The authors could not obtain pure $InCo_2O_4$ films because of significant phase segregation into Co_3O_4 and In_2O_3. Moreover, no structural data is available for $FeIn_2O_4$ and $MnIn_2O_4$, whose syntheses have not been yet reported, probably because their formation is thermodynamically unfavorable.

From the relatively large width of the XRD peaks, a nanostructured character of the powders can be inferred. The XRD patterns of In-TM oxides show broader peaks than those in undoped In_2O_3, suggesting smaller crystallite sizes. Interestingly, a shift in the position of the XRD peaks towards higher 2θ values is observed in the TM-doped oxides, particularly in Co-doped and Fe-doped ones, indicating a reduction in the cell parameter (see Figure 7a). The values of the crystallite sizes, cell parameters, atomic occupancies, and microstrains of the bixbyite, along with the weight percentages of the secondary oxide phases are listed in **Table 2** for the different SBA-15 and KIT-6 investigated mesoporous oxides.

In the TM-doped bixbyite phases, the crystallite size (or coherently diffracting length) ranges between 10 nm and 16 nm depending on both the doping element and the pore topology (i.e., SBA-15 or KIT-6). These values are considerably smaller than those in undoped In_2O_3 mesoporous structures. The crystallite sizes in the KIT-6 structures are systematically smaller than for the SBA-15 oxides. This is in agreement with the high-resolution TEM observations, as shown in Figure 2. Namely, while many of the SBA-15 nanowires were single crystalline or consisted of only a few crystallites, the KIT-6 frameworks were composed of plenty of nanocrystallites geometrically disposed in order to form the hexagonal pore arrangement. The microstrains were in the range of 2–4 $\times 10^{-3}$ for both the undoped and TM-doped mesoporous oxides.

© 2013 WILEY-VCH Verlag GmbH & Co. KGaA, Weinheim

Table 1. BET surface area and average pore size for the synthesized TM-doped In_2O_3 oxides calculated from the respective N_2 adsorption-desorption isotherms. "S" and "K" denote SBA-15 and KIT-6 mesostructures, respectively.

Material	BET Surface Area [$m^2\ g^{-1}$]	Average Pore Size [nm]
Co-doped (S)	64.5	7.1
Co-doped (K)	86.2	7.0
Fe-doped (S)	98.8	15.2
Fe-doped (K)	84.9	15.2
Mn-doped (S)	52.3	22.6
Mn-doped (K)	56.2	24.5

Remarkably, while the cell parameter of the bixbyite phase in the In-Mn oxide hardly varied compared with the undoped In_2O_3, a significant decrease was observed for In-Co and In-Fe oxides (see Table 2). Assuming that decomposition of the metal nitrates into the target mixed metal oxides occurs almost simultaneously, partial substitution of In^{3+} in the bixbyite lattice by Co, Fe, and Mn cations can be expected. Taking into account the ionic radius of Co^{2+} (0.63 Å) guest ion and that of the host In^{3+} ion (0.81 Å), one could anticipate a reduction in the cell parameter of the bixbyite phase due to heterovalent substitution. Furthermore, if we also consider the replacement of In^{3+} by Co^{3+} ions, isovalent substitution should also bring about a decrease in the cell parameter given the smaller ionic radius of Co^{3+} (0.525 Å) compared with In^{3+}.[53] The same reasoning

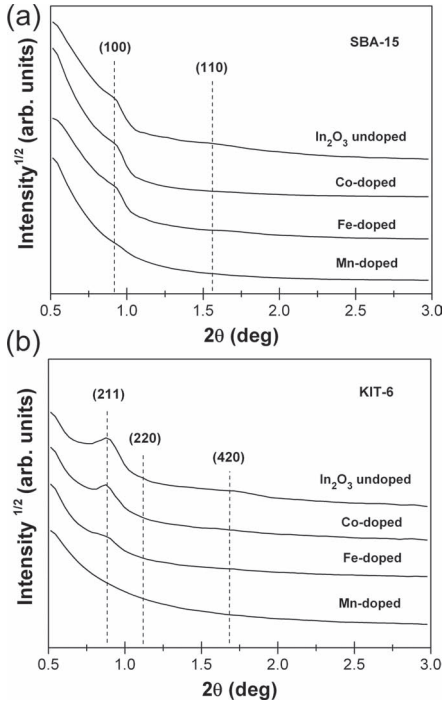

Figure 5. a,b) Low-angle XRD patterns corresponding to undoped In_2O_3, Co-doped, Fe-doped, and Mn-doped mesostructures obtained by nanocasting synthesis using SBA-15 (a) and KIT-6 silica (b) as hard templates.

accounts for Fe-In oxide (i.e., the isovalent substitution of In^{3+} by Fe^{3+} (0.64 Å) cations should cause a lattice contraction). Conversely, no significant changes in the cell parameters of the bixbyite phase was observed on comparing pure In_2O_3 and Mn-doped In_2O_3 mesoporous structures. In fact, In-Mn is a somewhat more complex case, given that a mixture of manganese oxides in several oxidation states is usually obtained by nanocasting.[51] Hence, both isovalent and heterovalent substitution might take place simultaneously (the ionic radii of Mn^{2+}, Mn^{3+}, and Mn^{4+} are 0.80 Å, 0.67 Å, and 0.54 Å, respectively), which ultimately makes the cell parameter change only slightly. The high XRD background for this system also suggests the presence of amorphous material, which further complicates the full-pattern fitting procedure.

From the relative intensity of the XRD peaks, Rietveld refinements also provide information on the atomic occupancies, as well as partial substitution of In^{3+} by the Co, Fe, or Mn cations. Interestingly, the fitting procedure revealed that, although virtually no vacancies were present in the cationic positions of the bixbyite phase, a significant amount of oxygen vacancies were formed during calcination, particularly in the SBA-15 mesoporous replicas. The values of the oxygen vacancies in the investigated materials are of the same order of magnitude as those reported in Co-doped In_2O_3 thin films prepared by pulse laser deposition.[54] Due to heterovalent cation substitution, the total oxygen content should decrease if the oxidation state of the guest ion is larger, in order to maintain charge balance. However, even in the undoped In_2O_3, oxygen vacancies were produced in considerable amounts. In fact, it has been reported that the number of oxygen vacancies in semiconductor In_2O_3 can be tailored post-synthesis by thermal annealing treatments, either in air or under a controlled Ar or O_2 atmosphere.[31,55–57] In our study, although calcinations were always performed in air, it is likely that access to O_2 inside the nitratre-filled pores of the silica templates was, to some extent, hindered, due in part to the release of NO_2 and/or NO_3 gases stemming from the oxidation reactions. As a result, oxygen-deficient $(In\text{-}TM)_2O_{3-y}$ mesoporous oxides were formed. Due to geometrical constraints, this effect could be exacerbated in the SBA-15 mesostructures, where guest gases such as O_2 can access the inner part of the silica network only from the open ends of the cylindrical pore channels.

As shown in Table 2, especially for the Fe- and Co-containing mesoporous materials, a considerable percentage of the In atomic positions in the bixbyite phase become occupied by the TM elements during calcination. Partial substitution of In^{3+} by Co or Fe cations is more pronounced in the SBA-15 than in the KIT-6 mesostructures, leading to a larger reduction in the cell parameter as compared with undoped In_2O_3. The TM cation occupancies in the In^{3+} positions reach 22% and 25% for the Co-doped and Fe-doped In_2O_3 SBA-15 structures, respectively. These values are close to the solubility limits reported for cobalt (20%)[57] and iron (20%[55,58] or 27.5%)[59] in the bixbyite phase. The occupancy of Mn cations in SBA-15 or KIT-6 mesostructures is smaller (≤8%), in agreement with the lower solubility limit reported for Mn in the In_2O_3 phase (i.e., 7.5%).[59] The rather low Mn occupancies are probably the reason for the higher cell parameters obtained in the $(In\text{-}Mn)_2O_{3-y}$ materials, in comparison with $(In\text{-}Co)_2O_{3-y}$ or $(In\text{-}Fe)_2O_{3-y}$. Taking these

© 2013 WILEY-VCH Verlag GmbH & Co. KGaA, Weinheim

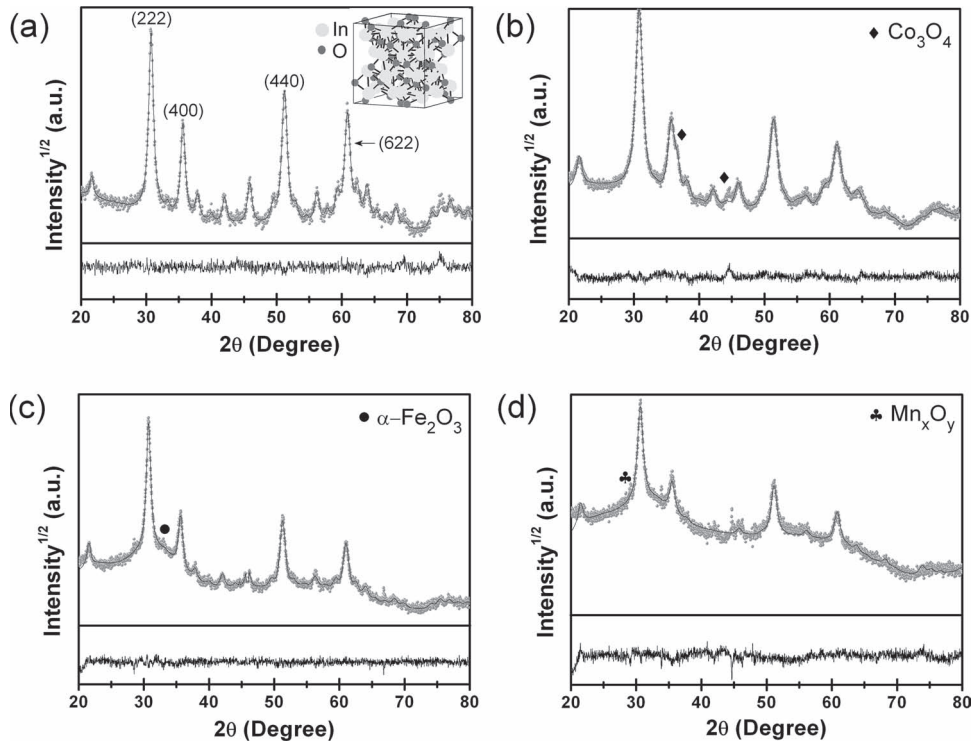

Figure 6. a–d) Experimental wide-angle XRD patterns (scatter) of pure In_2O_3 (a), Co-doped (b), Fe-doped (c), and Mn-doped (d) oxides obtained by nanocasting synthesis using KIT-6 silica as a template. The curves generated from the full-pattern Rietveld fitting (solid line) and the corresponding differences between the experimental and the calculated profiles (placed at the bottom) are also shown. The main peaks of the bixbyite phase are indexed in (a). The inset shows a schematic drawing of the unit cell. Some characteristic reflections of the secondary phases are indexed in (b-d).

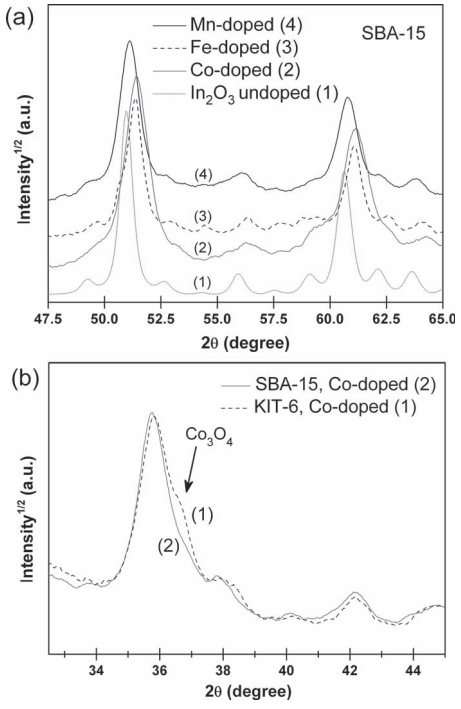

Figure 7. a,b) Wide-angle XRD patterns in the 47.5°–65° 2θ region of pure In_2O_3, Co-doped, Fe-doped and Mn-doped oxides obtained by nanocasting synthesis using SBA-15 silica as template (a); XRD patterns in the 32.5°–45° 2θ region of Co-doped In_2O_3 in the SBA-15 and KIT-6 mesostructures (b).

occupancy values into consideration, Table 2 also lists the stoichiometries proposed for the different mixed oxides.

When the bixbyite phase becomes saturated and further cation substitution is no longer possible, the excess Co, Fe, and Mn ions crystallize into their respective single oxides, resulting in the aforementioned formation of Co_3O_4, α-Fe_2O_3, and Mn_xO_y phases. As indicated in Table 2, the percentages of these phases do not exceed 15 wt% and their quantity is systematically larger in the KIT-6 structures, probably because of the lower doping-TM occupancies in the bixbyite phase observed in this case. Note that quantification of secondary phases could not be reliably performed for the (In-Mn) oxides due to the presence of the amorphous Mn_xO_y phases. Bearing in mind the initial 2:1 In:TM molar ratio used in the nitrate precursors, and once the real stoichiometry of the bixbyite phase has been determined for each TM-doped In_2O_3, it is possible to estimate the maximum amounts of secondary phases that form during the calcination processes. Using the atomic weights of the constituent elements, simple calculations predict 12.1% and 16.5% Co_3O_4 in the SBA-15 and KIT-6 structures, respectively, and 7.7% and 14.5% Fe_2O_3 for the SBA-15 and KIT-6 Fe-doped oxides, respectively. These values are close to those determined from the Rietveld refinements of the XRD data.

2.3. Magnetic Characterization

The hysteresis loops corresponding to the Co-, Fe-, and Mn-doped In_2O_3 SBA-15 and KIT-6 mesostructures, shown in

© 2013 WILEY-VCH Verlag GmbH & Co. KGaA, Weinheim

Table 2. Structural parameters obtained by Rietveld refinement of the XRD patterns of pure In_2O_3, and Co-doped, Fe-doped, and Mn-doped indium oxides obtained by nanocasting from SBA-15 (denoted as "S") and KIT-6 (denoted as "K") silica hosts.

Material	Cell parameter (±0.001) [Å]	Crystallite size (±1) [nm]	$\langle\varepsilon^2\rangle^{1/2}$ ($\pm 0.5\times10^{-3}$)	In1 + In2 occupancy (± 2) [%]	TM1 + TM2 occupancy (±2) [%]	Oxygen occupancy (±2) [%]	Resulting stoichiometry	Content of secondary phase (±0.5) [wt%]
Pure In_2O_3 (S)	10.112	25	3.0×10^{-3}	100	0	85	$In_2O_{2.55}$	0
Pure In_2O_3 (K)	10.119	19	2.5×10^{-3}	100	0	94	$In_2O_{2.82}$	0
Co-doped (S)	10.044	13	4.1×10^{-3}	78	22	92	$(In_{0.78}Co_{0.22})_2O_{2.76}$	11 (Co_3O_4)
Co-doped (K)	10.049	11	3.5×10^{-3}	84	16	98	$(In_{0.84}Co_{0.16})_2O_{2.94}$	15 (Co_3O_4)
Fe-doped (S)	10.050	16	3.0×10^{-3}	75	25	80	$(In_{0.75}Fe_{0.25})_2O_{2.4}$	7.5 (α-Fe_2O_3)
Fe-doped (K)	10.073	12	2.5×10^{-3}	85	15	95	$(In_{0.85}Fe_{0.15})_2O_{2.85}$	13 (α-Fe_2O_3)
Mn-doped (S)	10.103	12	2.0×10^{-3}	92	8	78	$(In_{0.92}Mn_{0.08})_2O_{2.34}$	–
Mn-doped (K)	10.108	10	1.5×10^{-3}	95	5	83	$(In_{0.95}Mn_{0.5})_2O_{2.49}$	–

Figure 8a,b, reveal that these materials exhibit a ferromagnetic behavior at room temperature, superimposed on a paramagnetic background. The ferromagnetic response is clearly evidenced in **Figure 9**, where the linear paramagnetic signal has been subtracted for all of the samples. The saturation magnetization achieved in the mesoporous TM-doped oxides is of the same order of magnitude as those reported in Co-doped, Fe-doped, or Ni-doped In_2O_3 thin films,[56,60] while the overall behavior (paramagnetic + ferromagnetic response) resembles very much that of Fe-doped In_2O_3 nanoparticles.[39] Remarkably, both the paramagnetic and ferromagnetic signals are more pronounced in the SBA-15 than for the KIT-6 structures, although the amounts of the secondary phases are larger in the latter. Furthermore, for both mesoporous structures, the magnetization in the Mn-doped semiconductors is lower than for the Co- and Fe-doped ones. These observations suggest that the incorporation of TMs into the In sites of the bixbyite phase has an influence on the observed magnetic properties. Since the solubility of Mn in bixbyite is rather limited, the resulting paramagnetic/ferromagnetic response is less prominent. However, it is worth mentioning that the undoped $In_2O_{3-\gamma}$ mesostructures also exhibit a small ferromagnetic behavior, with lower saturation magnetization than for the TM-doped oxides (see Figure 8c), but in this case the signal is superimposed to a diamagnetic background (i.e., with negative M vs. H slope). These observations are in agreement with other studies on undoped ODMS thin films, where the ferromagnetic properties have been attributed not to the presence of the doping elements, but to the oxygen vacancies.[45]

The origin of ferromagnetism in ODMSs is, in fact, a current topic of interest for many research groups, since contradictory results are often encountered in the literature, mainly depending on the material investigated (bulk-form, thin films, nanoparticles, …) and the synthesis methods used for sample preparation. Nevertheless, it is now generally accepted that oxygen vacancies contribute, to a large extent, to the observed ferromagnetic properties,[42,43,55] while X-ray magnetic circular dichroism studies have recently demonstrated that the TM doping ions mainly give a paramagnetic signal.[43,61] Some authors claim that metallic TM atomic clusters embedded in the ODMS could also give a ferromagnetic response.[62] This could indeed be the case in films prepared at room temperature by sputtering or other deposition techniques, but this possibility in our case is rather unlikely due to the conditions used during the calcination step (i.e., high temperatures and the presence of oxygen). Moreover, no evidence for metallic clusters was obtained, either by XRD or by TEM observations. The occurrence of secondary phases could still cause some of the observed magnetic effects. In particular, although α-Fe_2O_3 is antiferromagnetic, it cannot be ruled out that the formation of this phase could give rise to a weak ferromagnetic response at room temperature in the Fe-doped mesoporous structures.[47,63] However, the amount of α-Fe_2O_3 is significantly larger in the KIT-6 structure (almost by a factor of 2) than in the SBA-15 replica, whereas the hysteresis loops show much larger saturation magnetization for the SBA-15 oxide (see Figure 9b), indicating that the observed ferromagnetism cannot originate solely from the formation of α-Fe_2O_3 clusters. Furthermore, a ferromagnetic response of similar strength is observed in the Co-doped oxide mesostructures, although the secondary phase in this case (Co_3O_4) is paramagnetic at room temperature (its Néel temperature is around 30 K).[64] The case of the Mn-In mixed oxide is more complex since a mixture of Mn_xO_y phases are likely to form during the calcination process. It has been reported that Mn_3O_4 can crystallize in Mn-doped In_2O_3 powders if the amount of Mn is exceedingly large.[59] However, clear XRD peaks corresponding to this phase were not observed and, moreover, the Curie temperature of this ferrimagnetic phase is around 40 K. Hence, the eventual presence of Mn_3O_4 would not account for the room-temperature ferromagnetic behavior. In turn, most other Mn oxides (α-Mn_2O_3, β-MnO_2, MnO, …) are antiferromagnets with Néel temperatures between 90 K and 120 K.[65]

Nevertheless, it should be noted that a comprehensive interpretation of the magnetic behavior of substitutionally doped In_2O_3 is not simple when secondary phases are present in nanostructured form, as it occurs in our case. Indeed, it has been reported that many antiferromagnetic, diamagnetic and paramagnetic materials can show ferromagnetic-like behavior when prepared in the form of nanoparticles or ultrathin films. Hysteresis loops have been measured, for example, in antiferromagnetic NiO[66,67] and CoO nanoparticles,[68] in diamagnetic Au nanoparticles,[69] or in paramagnetic Pd nanoparticles,[70] amongst others. The occurrence of ferromagnetism in these

© 2013 WILEY-VCH Verlag GmbH & Co. KGaA, Weinheim

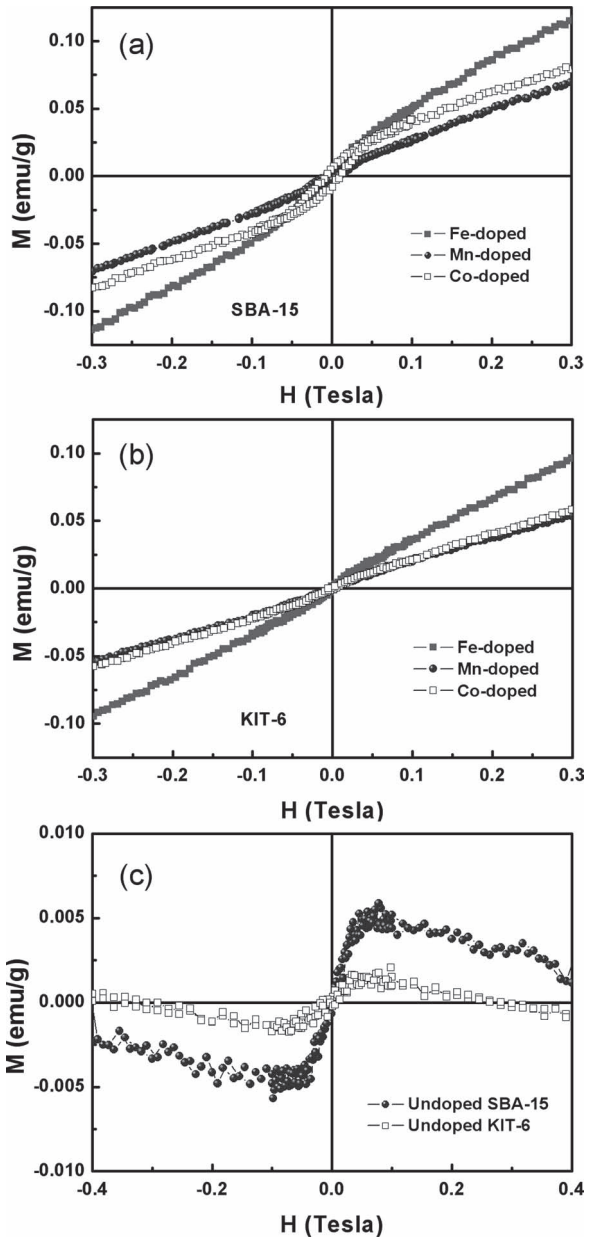

Figure 8. a–c) Hysteresis loops, measured at room temperature, corresponding to: the Co-doped, Fe-doped and Mn-doped In_2O_3 SBA-15 mesostructures (a); the Co-doped, Fe-doped and Mn-doped In_2O_3 KIT-6 mesostructures (b); and the undoped $In_2O_{3-\gamma}$ SBA-15 and KIT-6 mesoporous structures (c).

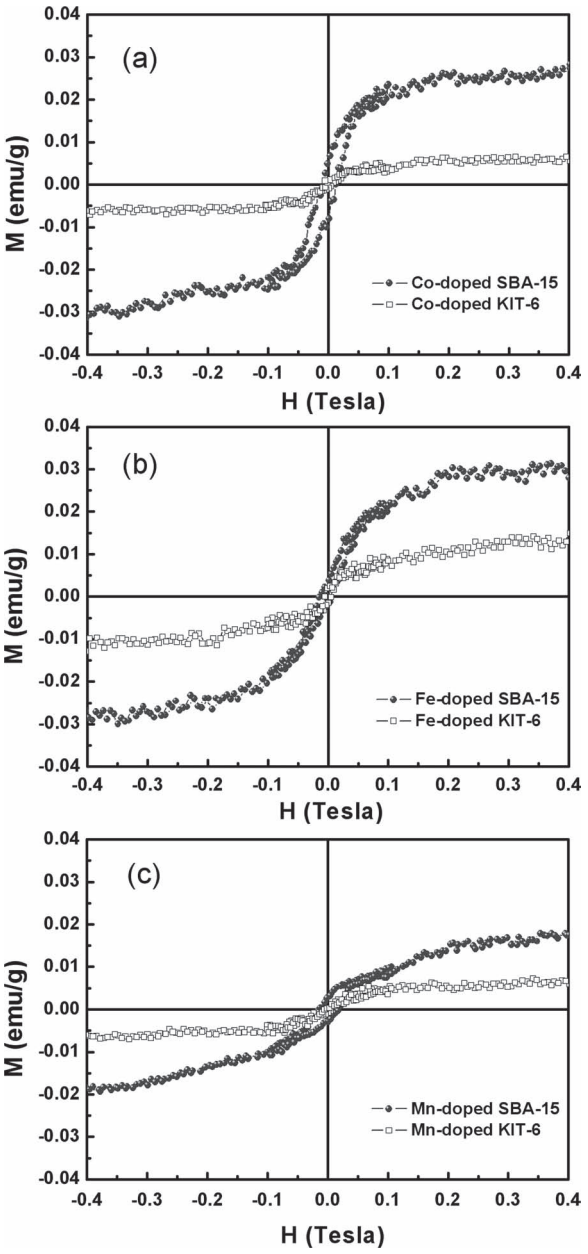

Figure 9. a–c) Normalized hysteresis loops (i.e., subtracting the paramagnetic background) corresponding to: the Co-doped In_2O_3 SBA-15 and KIT-6 mesoporous structures (a); the Fe-doped In_2O_3 SBA-15 and KIT-6 mesoporous structures (b); and the Mn-doped In_2O_3 SBA-15 and KIT-6 mesoporous structures (c).

nanoscale objects has been ascribed to a variety of factors: the existence of uncompensated surface spins in antiferromagnetic nanoparticles, electric interactions between diamagnetic or paramagnetic nanoparticles and surfactant molecules, and the occurrence of twinning and other crystallographic defects, etc. Because of these size effects, analysis of the physical origin of the ferromagnetic behavior of the mesoporous In-TM (TM = Co, Fe, Mn) composite oxides cannot completely rule out that the secondary phases contribute to some extent in the observed effects.

A mechanism based on ferromagnetic exchange interactions mediated by shallow donor electrons trapped in oxygen vacancies, which act as bound magnetic polarons, was proposed by Coey et al. to account for room-temperature ferromagnetism in dilute ferromagnetic oxides and nitrides.[35] First-principle energy-band calculations later showed that the donor impurities mainly consisted of hybridized 3d–4s TM-cation electronic states.[42] This model has been confirmed by a number of both theoretical and experimental studies.[28–36,43–46] In this sense, our observation of larger magnetization in the SBA-15

© 2013 WILEY-VCH Verlag GmbH & Co. KGaA, Weinheim

TM-doped mesostructures, where the number of oxygen vacancies and doping elements are larger, would also be in line with this theoretical framework.

In spite of the complexity of the physical origin of the observed magnetic effects, many applications have been envisaged from nanocomposite (i.e., not single phase) mesoporous oxide materials.[71] Actually, the combination of second-phase magnetic particles with semiconducting materials (i.e., magnetic-semiconductor nanocomposites) has been proposed for a variety of technological applications, including flash memories, low-current semiconductor lasers or single-photon emitters.[36] Furthermore, the newly developed mixed oxide mesostructures may also find applications in other fields, besides spintronics, such as catalysis or adsorption.

3. Conclusions

Porous Co-doped, Fe-doped, and Mn-doped indium oxides have been synthesized by nanocasting using SBA-15 and KIT-6 silica as templates. From the crystallographic viewpoint, the obtained powders consist of a mixture of bixbyite-type $(In_{1-x}TM_x)_2O_{3-y}$ oxides (formed as a result of partial cation substitution between the host In^{3+} and the guest Co, Fe, or Mn cations), together with minor amounts of secondary Co_3O_4/α-Fe_2O_3/Mn_xO_y phases. The In-Co and In-Fe oxide powders displayed the typical morphologies of SBA-15 and KIT-6 templated materials (i.e., the hexagonally arranged nanowires and the bicontinuous gyroid structure, respectively). Less-ordered mesophases were observed for the In-Mn oxide, as demonstrated by TEM and low-angle XRD analyses. The obtained mesoporous materials exhibit a room-temperature ferromagnetic behavior superimposed on a paramagnetic background. This has been attributed to the synergic effect of oxygen vacancies, together with the presence of TM doping cations in the bixbyite structure. Since In_2O_3 is a transparent semiconductor and these mesostructures are ferromagnetic, appealing magneto-optical and spintronic applications based on these geometrically ordered 3D engineered materials can be easily envisaged for the near future.

4. Experimental Section

Synthesis Details: Mesoporous silica SBA-15 was synthesized by dissolving Pluronic P123 copolymer (6.0 g) in diluted HCl. Tetraethyl orthosilicate (12.5 g), which served as the silicon source, was then added and the solution was stirred for 24 h at a constant temperature (37 °C). The hydrothermal treatment was carried out at 90 °C in a sealed container and the obtained solid was filtered, copiously washed with water and finally calcined at 550 °C for 5 h to remove the organics.

Mesoporous silica KIT-6 was synthesized under similar conditions, except for the addition of 1-butanol after dissolving the P123 surfactant. Stirring of the solution was carried out at 34 °C. Complete details of the silica syntheses can be found elsewhere.[4]

For the preparation of the In-TM (TM = Co, Fe, Mn) oxide replicas, the evaporation method was used as the impregnation step. $In(NO_3)_3{\cdot}xH_2O$, $Co(NO_3)_2{\cdot}6H_2O$, $Fe(NO_3)_3{\cdot}9H_2O$ and $Mn(NO_3)_2{\cdot}6H_2O$ salts (Sigma–Aldrich, 99.99% purity) were used as precursors. In brief, the mesoporous silica template (0.150 g) was put in contact with 1 mmol of metal nitrates (In:TM molar ratio of 2:1) in ethanol. The mixtures were stirred for 30 min in a crucible and left for ethanol evaporation overnight. The crucible was then placed in a tubular furnace and the impregnated silica was calcined. The furnace temperature was increased to 375 °C at a rate of 3 °C min^{-1} and held at this temperature for 4 h under atmospheric conditions. At the end of this process, the furnace was slowly cooled down to room temperature. The silica host was removed with 30 mL of 2 M NaOH solution at 70 °C under stirring for 24 h. The resulting mesoporous replicas were collected after centrifugation and decanted off the supernatant, copiously rinsed in ethanol, and finally dried.

Characterization: The morphology and chemical composition of the materials was investigated by transmission electron microscopy (TEM) using a Jeol-JEM 2011 system operated at 200 kV, and field-emission scanning electron microscopy (FE-SEM) using a Merlin Zeiss microscope operated at 2 kV, and equipped with energy dispersive X-ray (EDX) compositional analysis. Samples for the TEM observations were prepared by dispersing a small amount of powder in ethanol and then one or two drops of the suspension were placed dropwise onto a holey carbon-supported grid. For FE-SEM characterization, the powders were spread onto a silicon substrate and directly imaged under the electron beam. Brunauer–Emmet–Teller (BET) surface area analyses were performed using a Micromeritics ASAP 2020 instrument. N_2 adsorption/desorption isotherms were recorded at 77 K after degassing the powders at 175–200 °C for 10 h. The pore sizes were estimated by applying the Barrett–Joyner–Halenda (BJH) algorithm to the desorption branches. Low-angle X-ray diffraction (XRD) patterns were acquired using a Panalytical X'Pert Pro diffractometer in the 0.5–3° 2θ angular range operating in transmission mode using Cu Kα radiation. Wide-angle XRD patterns were collected on a Philips X'Pert diffractometer in the 20–80° 2θ range (step size = 0.03°, step time = 10 s) using Cu Kα radiation. The structural parameters (crystallite size, microstrains, cell parameter, atomic occupancies, and phase percentages) were evaluated by fitting the full XRD patterns using the materials analysis using diffraction (MAUD) Rietveld refinement software.[71–74] Hysteresis loops were recorded at room temperature using an Oxford Instruments vibrating-sample magnetometer (VSM), with a maximum applied magnetic field of 0.4 T.

Supporting Information

Supporting Information is available from the Wiley Online library or from the author.

Acknowledgements

The authors sincerely thank BASF Corporation for kindly supplying the P123 precursor used for mesoporous silica synthesis. This work was supported by the 2009-SGR-1292 project of the Generalitat de Catalunya and the MAT2010-20616-C02-02 and MAT2011-27380-C02-01 projects from the Spanish Ministry of Science and Innovation (MICINN). We thank MATGAS 2000 AIE for the provision of their facilities and technical assistance in the BET experiments. We also thank Dr. Sebastiano Garroni for his valuable help in the BET experiments. M.D.B. was partially supported by an ICREA ACADEMIA award.

Received: June 2, 2012
Published online: September 28, 2012

[1] *The Chemistry of Nanomaterials: Synthesis, Properties and Applications*, (Eds: C. N. R. Rao, M. L. Achim, A. K. Cheetham, Wiley-VCH, WeinheimGermany **2005**.
[2] J. Liu, S. Z. Qiao, Q. H. Hu, G. Q. (Max) Lu, *Small* **2011**, *7*, 425.
[3] *Nanocasting. A Versatile Strategy for Creating Nanostructured Porous Materials*, (Eds: A. H. Lu, D. Zhao, Y. Wan) RSC Publishing, Cambridge, UK **2010**.

© 2013 WILEY-VCH Verlag GmbH & Co. KGaA, Weinheim

[4] M. Cabo, E. Pellicer, E. Rossinyol, O. Castell, S. Suriñach, M. D. Baró, *Cryst. Growth. Des.* **2009**, *9*, 4814.
[5] J. Zhu, Q. Gao, *Microporous Mesoporous Mater.* **2009**, *124*, 144.
[6] Y. Sun, G. Ji, M. Zheng, X. Chang, S. Li, Y. Zhang, *J. Mater. Chem.* **2010**, *20*, 945.
[7] A. H. de Morais Batista, F. S. O. Ramos, T. P. Braga, C. L. Lima, F. F. de Sousa, E. B. D. Barros, J. M. Filho, A. S. de Oliveira, J. R. de Sousa, A. Valentini, A. C. Oliveira, *Appl. Catal. A* **2010**, *382*, 148.
[8] M. Gu, B. Yue, R. Bao, H. He, *Mater. Res. Bull.* **2009**, *44*, 1422.
[9] P. F. Fulvio, A. Vinu, M. Jaroniec, *J. Phys. Chem. C* **2009**, *113*, 13565.
[10] J. Zhu, Q. Gao, Z. Chen, *Appl. Catal. B* **2008**, *81*, 236.
[11] M. Cabo, E. Pellicer, E. Rossinyol, M. Estrader, A. López-Ortega, J. Nogués, O. Castell, S. Suriñach, M. D. Baró, *J. Mater. Chem.* **2010**, *20*, 7021.
[12] Y. Rao, D. M. Antonelli, *J. Mater. Chem.* **2009**, *19*, 1937.
[13] G. Korotcenkov, B. K. Choc, *Crit. Rev. Solid State Mater. Sci.* **2010**, *35*, 1.
[14] P. G. Bruce, B. Scrosati, J.-M. Tarascon, *Angew. Chem. Int. Ed.* **2008**, *47*, 2930.
[15] J. Haetge, P. Hartmann, K. Brezesinski, J. Janek, T. Brezesinski, *Chem. Mater.* **2011**, *23*, 4384.
[16] Y. Lei, C. Fournier, J.-L. Pascal, F. Favier, *Microporous Mesoporous Mater.* **2008**, *110*, 167.
[17] H. Luo, J. Zhang, Y. Yan, *Chem. Mater.* **2003**, *15*, 3769.
[18] B. Tian, X. Liu, L. A. Solovyov, Z. Liu, H. Yang, Z. Zhang, S. Xie, F. Zhang, B. Tu, C. Yu, O. Terasaki, D. Zhao, *J. Am. Chem. Soc.* **2004**, *126*, 865.
[19] S. Haffer, T. Waitz, M. Tiemann, *J. Phys. Chem. C* **2010**, *114*, 2075.
[20] S.-C. Chang, M. H. Huang, *J. Phys. Chem. C* **2008**, *112*, 2304.
[21] A. Prim, E. Pellicer, E. Rossinyol, F. Peiró, A. Cornet, J. R. Morante, *Adv. Funct. Mater.* **2007**, *17*, 2957.
[22] X. Lai, D. Wang, N. Han, J. Du, J. Li, C. Xing, Y. Chen, X. Li, *Chem. Mater.* **2010**, *22*, 3033.
[23] T. Waitz, T. Wagner, T. Sauerwald, C.-D. Kohl, M. Tiemann, *Adv. Funct. Mater.* **2009**, *19*, 653.
[24] X. Liu, R. Wang, T. Zhang, Y. He, J. Tu, X. Li, *Sens. Actuators B* **2010**, *150*, 442.
[25] H. Zhou, W. Cai, L. Zhang, *Appl. Phys. Lett.* **1999**, *75*, 495.
[26] H. Yamaura, J. Tamaki, K. Moriya, N. Miura, N. Yamazoe, *J. Electrochem. Soc.* **1997**, *144*, L158.
[27] M. I. Ivanovskaya, D. A. Kotsikau, A. Taurino, P. Siciliano, *Sens. Actuators B* **2007**, *124*, 133.
[28] Y. Matsumoto, M. Murakami, T. Shono, T. Hasegawa, T. Fukumura, M. Kawasaki, P. Ahmet, T. Chikyow, S.-Y. Koshihara, H. Koinuma, *Science* **2001**, *291*, 854.
[29] D. Maestre, I. Martínez de Velasco, A. Cremades, M. Amati, J. Piqueras, *J. Phys. Chem. C* **2010**, *114*, 11748.
[30] H. Takizawa, K. Uheda, T. Endo, *J. Mater. Sci. Lett.* **2001**, *20*, 359.
[31] J. Philip, A. Punnoose, B. I. Kim, K. M. Reddy, S. Layne, J. O. Holmes, B. Satpati, P. R. Leclair, T. S. Santos, J. S. Moodera, *Nat. Mater.* **2006**, *5*, 298.
[32] N. H. Hong, J. Sakai, N. T. Huong, A. Ruyter, V. Brizé, *J. Phys.: Condens. Matter* **2006**, *18*, 6897.
[33] P. Sharma, A. Gupta, K. V. Rao, F. J. Owens, R. Sharma, R. Ahuja, J. M. Osorio Guillen, B. Johansson, G. A. Gehring, *Nat. Mater.* **2003**, *2*, 673.
[34] P. I. Archer, P. V. Radovanovic, S. M. Heald, D. R. Gamelin, *J. Am. Chem. Soc.* **2005**, *127*, 14479.
[35] J. M. D. Coey, M. Venkatesan, C. B. Fitzgerald, *Nat. Mater.* **2005**, *4*, 173.
[36] T. Dietl, *Nat. Mater.* **2010**, *9*, 965.
[37] S. S. Farvid, L. Ju, M. Worden, P. V. Radovanovic, *J. Phys. Chem. C* **2008**, *112*, 17755.
[38] S. S. Farvid, N. Dave, T. Wang, P. V. Radovanovic, *J. Phys. Chem. C* **2009**, *113*, 15928.
[39] A. Singhal, S. N. Achary, J. Manjanna, O. D. Jayakumar, R. M. Kadam, A. K. Tyagi, *J. Phys. Chem. C* **2009**, *113*, 3600.
[40] J. S. Kulkarni, O. Kazakova J. D. Holmes, *Appl. Phys. A* **2006**, *85*, 277.
[41] Y.- W. Jun, Y.-Y. Jung, J. Cheon, *J. Am. Chem. Soc.* **2002**, *124*, 615.
[42] S. J. Hu, S. S. Yan, X. L. Lin, X. X. Yao, Y. X. Chen, G. L. Liu, L. M. Mei, *Appl. Phys. Lett.* **2007**, *91*, 262514.
[43] A. M. H. R. Hakimi, F. Schoofs, R. Bali, N. A. Stelmashenko, M. G. Blamire, S. Langridge, S. A. Cavill, G. van der Laan, S. S. Dhesi, *Phys. Rev. B: Condens. Matter* **2010**, *82*, 144429.
[44] A. M. H. R. Hakimi, M. G. Blamire, S. M. Heald, M. S. Alshammari, M. S. Alqahtani, D. S. Score, H. J. Blythe, A. M. Fox, G. A. Gehring, *Phys. Rev. B: Condens. Matter* **2011**, *84*, 085201.
[45] N. H. Hong, J. Sakai, N. Poirot, V. Brizé, *Phys. Rev. B: Condens. Matter* **2006**, *73*, 132404.
[46] D. Bérardan, E. Guilmeau, *J. Phys.: Condens. Matter* **2007**, *19*, 236224.
[47] F. Jiao, A. Harrison, J.-C. Jumas, A. V. Chadwick, W. Kockelmann, P. G. Bruce, *J. Am. Chem. Soc.* **2006**, *128*, 5469.
[48] F. Jiao, A. Harrison, A. H. Hill, P. G. Bruce, *Adv. Mater.* **2007**, *19*, 4063.
[49] F. Jiao, A. H. Hill, A. Harrisson, A. Berko, A. V. Chadwick, P. G. Bruce, *J. Am. Chem. Soc.* **2008**, *130*, 5262.
[50] H. Tüysüz, M. Comotti, F. Schüth, *Chem. Commun.* **2008**, 4022.
[51] M. Imperor-Clerc, D. Bazin, M. D. Appay, P. Beaunier, A. Davidson, *Chem. Mater.* **2004**, *16*, 183.
[52] A. Walsh, K. S. Ahn, S. Shet, M. N. Huda, T. G. Deutsch, H. Wang, J. A. Turner, S.-H. Wei, Y. Yan, M. M. Al-Jassim, *Eng. Environ. Sci.* **2009**, *2*, 774.
[53] S. Y. Istomin, V. A. Koutcenko, E. V. Antipov, G. Svensson, J. P. Attfield, *J. Mater. Chem.* **2002**, *12*, 2352.
[54] N. H. Hong, J. Sakai, N. T. Hong, V. Brizé, *J. Magn. Magn. Mater.* **2006**, *302*, 228.
[55] P. F. Xing, Y. X. Chen, S. S. Yan, G. L. Liu, L. M. Mei, Z. Zhang, *J. Appl. Phys.* **2009**, *106*, 043909.
[56] J. Stankiewicz, F. Villuendas, J. Bartolomé, *Phys. Rev. B: Condens. Matter* **2007**, *75*, 235308.
[57] G. Subías, J. Stankiewicz, F. Villuendas, M. P. Lozano, J. García, *Phys. Rev. B: Condens. Matter* **2009**, *79*, 094118.
[58] J. He, S. Xu, Y. K. Yoo, Q. Xue, H. C. Lee, S. Cheng, X. D. Xiang, G. F. Dionne, I. Takeuchi, *Appl. Phys. Lett.* **2005**, *86*, 052503.
[59] D. Bérardan, E. Guilmeau, D. Pelloquin, *J. Magn. Magn. Mater.* **2008**, *320*, 983.
[60] X. Li, C. Xia, G. Pei, X. He, *J. Phys. Chem. Sol.* **2007**, *68*, 1836.
[61] N. H. Hong, A. Barla, J. Sakai, N. Q. Huong, *Phys. Status Solidi C* **2007**, *4*, 4461.
[62] D. H. Kim, J. S. Yang, K. W. Lee, S. D. Bu, T. W. Noh, S. J. Oh, Y. W. Kim, J. S. Chung, H. Tanaka, H. Y. Lee, T. Kawai, *Appl. Phys. Lett.* **2002**, *81*, 2421.
[63] A. H. Hill, F. Jiao, P. G. Bruce, A. Harrison, W. Kockelmann, C. Ritter, *Chem. Mater.* **2008**, *20*, 4891.
[64] Y. Ichiyanagi, Y. Kimishima, S. Yamada, *J. Magn. Magn. Mater.* **2004**, *272–276*, e1245.

© 2013 WILEY-VCH Verlag GmbH & Co. KGaA, Weinheim

[65] T. Ahmad, K. V. Ramanujachary, S. E. Lofland, A. K. Ganguli, *J. Mater. Chem.* **2004**, *14*, 3406.
[66] R. H. Kodama, S. A. Makhlouf, A. E. Berkowitz, *Phys. Rev. Lett.* **1997**, *79*, 1393.
[67] S. Mandal, K. S. R. Menon, S. K. Mahatha, S. Banerjee, *Appl. Phys. Lett.* **2011**, *99*, 232507.
[68] X. He, H. Shi, *Mater. Res. Bull.* **2011**, *46*, 1692.
[69] P. Crespo, R. Litrán, T. C. Rojas, M. Multigner, J. M. de la Fuente, J. C. Sánchez-López, M. A. García, A. Hernando, S. Penadés, A. Fernández, *Phys. Rev. Lett.* **2004**, *93*, 087204.
[70] B. Sampedro, P. Crespo, A. Hernando, R. Litrán, J. C. Sánchez López, C. López Cartes, A. Fernandez, J. Ramírez, J. González Calbet, M. Vallet, *Phys. Rev. Lett.* **2003**, *91*, 237203.
[71] J.-L. Shi, Z.-L. Hua, L.-X. Zhang, *J. Mater. Chem.* **2004**, *14*, 795.
[72] L. Lutterotti, R. Ceccato, R. Dal Maschio, E. Pagani, *Mater. Sci. Forum* **1998**, *278–281*, 87.
[73] J. Sort, J. Nogués, S. Suriñach, M. D. Baró, *Philos. Mag.* **2003**, *83*, 439.
[74] This program can be downloaded from http://www.ing.unitn.it/~maud/ (accessed September 2012).

© 2013 WILEY-VCH Verlag GmbH & Co. KGaA, Weinheim